International Symposium
On Turbulence and Shear Flow
Phenomena (TSFP-9)
June 30 - July 3, 2015 *Melbourne, Australia*

Tomographic-PIV investigation of turbulent structures over nano-fabricated superhydrophobic surfaces

Sina Rafati
Department of Mechancial Engineering
University of Alberta
Canada, Edmonton AB T6G 2G8
rafati1@ualberta.ca

Abdul Wasay
Department of Mechancial Engineering
University of Alberta
Canada, Edmonton AB T6G 2G8
wasay@ualberta.ca

Dan Sameoto
Department of Mechancial Engineering
University of Alberta
Canada, Edmonton AB T6G 2G8
sameoto@ualberta.ca

Sina Ghaemi
Department of Mechancial Engineering
University of Alberta
Canada, Edmonton AB T6G 2G8
ghaemi@ualberta.ca

ABSTRACT

The effect superhydrophobic (SHO) surfaces with different micro-size surface patterns on the flow structure of a turbulent channel flow at Reynolds number of 10,500 is investigated. Three surfaces with spanwise, streamwise, and hexagonal micro-size features along with a reference smooth surface are flush mounted in a flow loop with rectangular cross-section of 40×6 mm^2. Measurements are conducted using planar particle image velocimetry (PIV) at magnification of M = 0.8 and planar particle tracking velocimetry (PTV) at M = 2.9. Profiles of mean velocity and turbulent intensities show that the surface with spanwise microgrooves has the highest skin friction. The hexagonal surface has slightly higher skin-friction in comparison with the smooth and the streamwise microgroove surfaces, which performed identically. The results demonstrate that the air layer of the SHO surface did not last under the turbulent flow and the surfaces are wetted at the current experimental condition. Measurement of the three-dimensional turbulent structures using tomographic particle image velocimetry (Tomo-PIV) and three-dimensional PTV (3D-PTV) at high spatial-resolution of 132 voxel/mm and M = 0.9 is evaluated. The Tomo-PIV underestimated turbulent intensities due to the large windows of $27.9^+ \times 27.9^+ \times 27.9^+$ (normalized with the wall unit) while the 3D-PTV provides an accurate measurement of $\langle u^2 \rangle$ and $\langle v^2 \rangle$. The 3D-PTV overestimates $\langle w^2 \rangle$ due to higher noise level of the out-of-plane velocity component.

INTRODUCTION

Reduction of skin-friction in turbulent wall flows can improve the efficiency of a wide range of industrial systems from hydro-transport pipelines to marine and aeronautical systems. A viable method of friction reduction has emerged due to the recent development of nanofabrication technology enabling production of micron/nanoscale surface patterns. These patterns along with the chemical hydrophobicity of the substrate introduce the superhydrophobic (SHO) surfaces, which is characterized by water droplet contact angles higher than 150°. Superhydrophobicity prevents the liquid flow from wetting the cavities of the micro/nano scale pattern of the SHO surfaces. As a result, the surface would be covered by micro/nano air pockets forming liquid-air interface instead of the liquid-solid interface as shown in Figure 1. The stability of this air-liquid interface follows Young's law that provides a relationship between the pressure difference at the liquid/air interface and the liquid surface tension (Choi et al., 2006).

Experimental investigations have demonstrated an apparent slip at the SHO surface and friction reduction up to 40 percent in the laminar regime (Ou and Rothestin 2005; Maynes et al. 2007). The shear-free boundary condition and the Naviers' slip model may suggest that the reduction of friction is independent of the flow regime. However, *Re* number dependence has been observed in the previous experimental investigations in the turbulent regime. Daniello et al. (2009) proposed a critical *Re* number for the onset of drag reduction. They argue that the scale of the viscous sublayer should be smaller than the scale of the micro-features of the SHO to obtain any drag reduction. In contrary, Henoch et al. (2006), Watanabe et al. (1999), and Davis et al. (2006) reported lower friction reduction with increase of *Re* number. The apparent contradictory dependence on *Re* motivates further investigation into the behavior of SHO surfaces at the turbulent regime.

SHO surfaces are classified into random and ordered patterns. The random patterns are typically fabricated using the spray coating technique. Although suitable for large-scale turbulent applications, the random and hierarchical surface makes a systematic investigation of the effect of surface topology difficult. On the other hand, the ordered patterns are typically produced using detailed nano-fabrication techniques ensuring control over the surface features. The SHO surfaces with ordered patterns require a more complex manufacturing process, limiting the application to small scale micro-fluidic applications. There have been a few investigations on turbulent flow over SHO

surfaces with ordered patterns confirming extension of friction reduction at high Re numbers along with *Re* dependent behavior (Park et al. 2014).

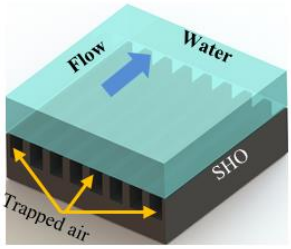

Figure 1. A schematic of the liquid phase over a SHO surface. Trapped air in the micro grooves forms the air-liquid interface with shear-free boundary condition.

Detailed investigation of the effect of the surface pattern on the turbulent structure has been mostly carried out with the aid of numerical simulations. Direct numerical simulation (DNS) of Min and Kim (2004) showed reduction of friction with streamwise slip boundary condition while the spanwise slip boundary condition increased the skin friction. The latter is associated with the intensification of turbulence intensities and streamwise vortices. Martell et al. (2009) simulated micro-posts and micro-ridges geometries of the superhydrophobic surface in a DNS simulation. They showed larger reduction of friction by increasing the micro-features spacing up to 90 μm and associated the gain with larger shear-free surface. In practice, the large micro-features are prone to wettability and suffer from longevity of the air-liquid interface. The performance of patterned SHO surfaces is extremely complex due to the possible involvement of surface compliance, attenuation of turbulent structures, and possible wettability of the micro-size cavities under a turbulent flow. In this work, the effect of different micro-size surface patterns (streamwise, spanwise and hexagonal) on the turbulent flow structures and the possible wettability of the air pockets are experimentally investigated. Planar PIV and high spatial-resolution PTV is applied to characterize the profiles of mean velocity and Reynolds stresses in the near wall region. Volumetric measurements using Tomo-PIV and 3D-PTV are also evaluated for future investigation of the three-dimensional turbulent structures.

EXPERIMENTAL SETUP

Flow Facility

The experiments are performed in a closed-circuit water channel with a rectangular cross-section of 40×6 mm^2 (W×H) developed for the study of the SHO surfaces. The aspect ratio of the cross-section is 6.7 and the hydraulic diameter is 10.4 mm. The total length of the rectangular channel is 1200 mm (200H) and the SHO surfaces were installed at 720 mm (120H) from the channel entrance to ensure fully developed channel flow over SHO surfaces. Figure 2 shows the test section and the upstream settling chamber of the facility. The upstream chamber has large cross-section which includes a honeycomb and a fine mesh followed by a contraction section (22:1). The top plate of the test section consists of a replaceable module with flush mounted SHO surfaces. The bottom and top plates are made from the cast acrylic and the side walls are made from glass for high quality optical access.

The flow is circulated using a gear pump and controlled by a variable frequency driver. A magnetic flow meter (Omega, FLR 7320D) is used to monitor the mass flow rate. The working fluid is deionized water seeded with silver-coated 2 μm spherical glass bead particles (Potters Industries).

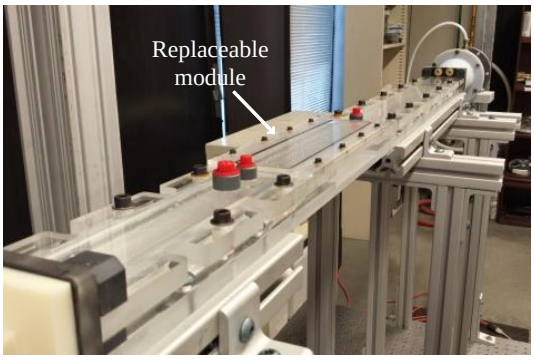

Figure 2. An image of the flow loop showing the fully transparent test section and the replacable module.

SHO Surfaces

In order to evaluate the effect of surface pattern, three SHO surfaces with streamwise and spanwise grooves and hexagonal cavities were manufactured as illustrated in Figure 3. Piranha cleaned wafer was photo lithographically patterned and Deep Reactive Ion Etching was performed to a suitable depth. The wafers were then silane treated to induce hydrophobicity. All three surfaces have approximately the same ratio of cavity over solid surface of 50 percent. The SHO surfaces were fabricated in the nano-fabrication laboratory of the University of Alberta. From each SHO pattern, three 36×78 mm^2 surfaces were fabricated and installed into the replaceable module of the channel. The details of SHO surfaces are summarized in Table 1. An acrylic surface is also considered as the smooth reference surface.

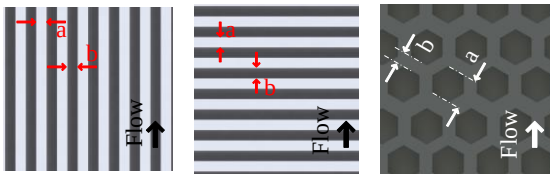

Figure 3. The patterned SHO surfaces including (a) streamwise grooves, (b) spanwise grooves, and (c) the hexagonal pattern.

Table 1. Micro-scale features of the SHO patterns of Figure 3. Parameter c is the wall-normal depth of the features.

SHO	*a (μm)*	*b* (μm)	*c* (μm)
streamwise	15	15	30
spanwise	15	15	30
hexagonal	95	50	30

Planar PIV/PTV

Two separate planar measurement systems are considered; (a) a low magnification (M = 0.8) system (LMS) covering the full channel height for PIV processing and (b) a high magnification (M = 2.9) system (HMS) for the near wall measurement using PTV. For this purpose, two Imager Intense cameras (1040×1376 px^2 and 12-bit resolution) and an Nd:YAG laser (Solo III-15, New Wave Research) were utilized as shown in Figure 4. The laser delivers maximum of 50 mJ over 3-4 ns pulse width at 532 nm wavelengths. A thin laser sheet of 0.5-1 mm thickness was formed in the field-of-view of cameras using a combination of cylindrical and spherical lenses. The low magnification camera is equipped with a Nikkor SLR objective with focal length of 105 mm at f/11. The high magnificent camera is equipped with a long-range microscope (12X zoomlens, Navitar). The fields-of-view of the low and high magnification systems were 6.7×8.9 mm^2 and 3.1×2.4 mm^2 with a digital image resolution of 160 and 440 pixel/mm, respectively. PIV recordings are obtained using double-frame mode. The two laser pulses are synchronized with the camera frames using a programmable timing unit (Lavision GmbH, PTU9) controlled by DaVis 8.2. The time separation between two laser pulses is 63 and 27 μs for the low and high magnification systems, respectively. An ensemble of 10,000 image pairs was recorded for each measurement.

The minimum intensity of the ensemble of images was subtracted from the individual images followed by normalization by the average of the ensemble images. The mean velocity field is obtained using the ensemble of correlations technique (Meinhart et al., 2000) applied to interrogation windows of 8×8 px^2 with 75 percent overlap. The turbulent intensities are obtained from individual cross-correlation of the double-frame images using a multi-pass algorithm with final interrogation windows of 32×32 px^2 with 75 percent overlap. All the PIV processing are carried out in Davis 8.2 (LaVision).

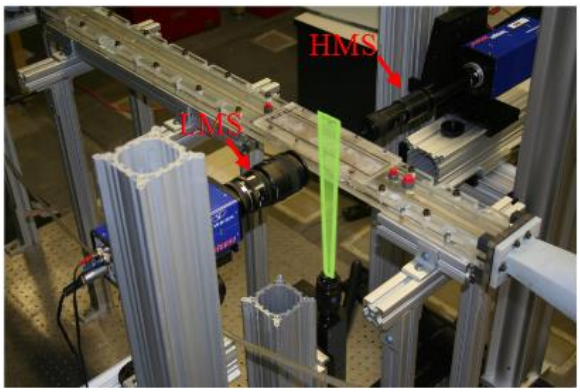

Figure 4. Planar PIV/PTV showing the laser sheet illuminating a wall-normal streamiwse plane. The camera on the left side covers the full channel (LMS) and the camera on the right side covers the near-wall region (HMS).

Measure of the flow motion in the vicinity of the wall requires high spatial resolution achievable using particle tracking velocimetry (Kähler et al., 2012). A PTV code is developed in MATLAB which initially detects particles based on a preliminary intensity threshold. A Gaussian filter was applied to the detected particles followed by removal of overlap particles and out-of-focus and distorted particles. An initial average vector field obtained using the ensemble of correlation technique is used to detect the particle pairs. The PTV results were averaged over 12 pixel wall-normal windows for statistical convergence.

Volumetric PIV/PTV

Volumetric measurement is carried out by a combination of Tomo-PIV and 3D-PTV techniques. The illumination of the volumetric measurements is provided by the Nd:YAG laser (Solo III-15, New Wave Research). In this measurement, a collimated laser sheet is expanded in the spanwise direction (z) to a thickness of 3 mm. A knife edge filter with width of 3mm was attached to the bottom surface of the channel to cut off the low-energy tail of the expanded laser sheet and obtain a top-hat light intensity profile.

Imaging system consists of four CCD cameras (Imager ProX, LaVisison) with 2048×2048 px^2 sensor. The cameras were equipped with scheimpflug adapters and 105 mm Nikkor SLR objective with an aperture setting of f / 22 as shown in Figure 5. The measurement volume is 15.5×10×3 mm^3 (1971×723×394 voxel^3) with magnification and spatial resolution of M = 0.9 and S = 132 voxel/mm, respectively. The synchronization between laser and the cameras is provided by a programmable timing unit (PTU9, LaVision, GmbH). The solid angle of two left cameras is 50 degrees and the solid angle of the two right cameras is 30 degrees as shown in Figure 5. Ensembles of 4,000 double-frame images were recorded for each volumetric measurement.

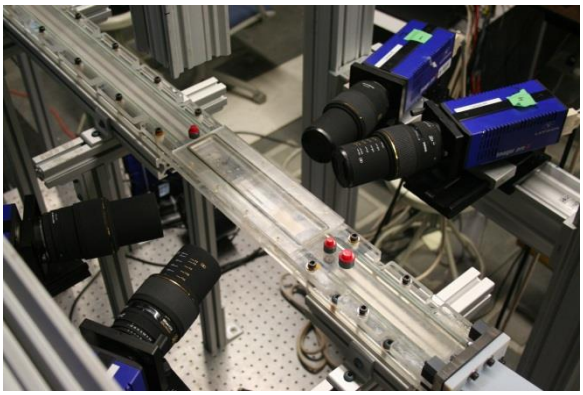

Figure 5. Experimental setup of the Tomo-PIV/PTV showing four cameras imaging a streamiwse wall-normal field of view with 3 mm thickness in the depth direction (spanwise).

The initial mapping function of the tomographic system is obtained using a pinhole model on a two-dimensional target with 0.3 mm dotes spaced 2 mm apart. The target is traversed with 0.5 mm steps in the spanwise direction of the channel. The volume-self-calibration technique (Wienke, 2008) was applied to reduce the residual RMS of the disparity map from 1-2 pixels in the physical calibration stage to 0.02-0.05 pixels. The illuminated volume has been seeded with 2μm silver coated glass beads at a concentration of approximately 200-250 particles/mm^3 with

a particle image number density of approximately 0.015 particles per pixel (ppp).

Images are preprocessed by subtracting the minimum of the ensemble images followed by normalization by the average intensity. The signal-to-noise ratio of the images is further improved by subtracting the local minimum and intensity normalization using a local average (kernel of 51 pixels). The three-dimensional location of the particles was reconstructed with iterative multiplicative algebraic reconstruction (MART, Herman & Lent 1976). The volumetric cross-correlation is performed using multi-pass algorithm with final interrogation volume size of 48×48×48 voxel^3 (0.36×0.36×0.36 mm^3) with 75 percent overlap. Davis 8.2 (LaVision, GmbH) is used for image acquisition and all processing. The performance of the tomographic reconstruction process is evaluated through the light intensity distribution cross the depth of a reconstructed volume. The ratio of reconstructed light intensity (I_R) within the illuminated region to the light intensity outside of the reconstructed volume is about 2.5 in Figure 6. Moreover, the depth of the reconstructed volume is about 3 mm compatible with the width of the laser sheet. The divergence of the velocity field $\nabla.\vec{V}$ is estimated about 0.04 voxel/voxel which shows the accuracy of the three-dimensional velocity field against the local conservation of mass.

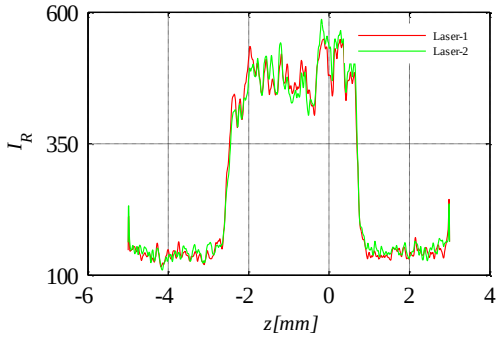

Figure 6. The average intensity profile along the z-axis (depth) of the reconstructed tomographic volume.

The 3D-PTV algorithm of Davis 8.2 is applied to the double-frame images of the four cameras using the same mapping function obtained from the physical and self-calibration procedure of the Tomo-PIV. Maximum triangulation error of 2 pixel is applied to detect the location of the particles (3-5 pixels diameter) in the three-dimensional space.

RESULTS AND DISCUSSION

Planar PIV and PTV

The normalized mean velocity profile from planar LMS PIV, processed by the ensemble of correlations, is shown in Figure 7. The velocity profiles of the magnified view show slightly smaller mean velocity for the spanwise micro-grooved surface while the other profiles almost overlap. Detailed characterization of the sublayer and wall shear stress is difficult due to the thin sublayer (about 0.002H) and uncertainties in estimation of the wall location.

Planar PTV is applied to scrutinize the near wall mean velocity profile with higher spatial resolution. The results are shown in Figure 8 captures the small near wall curvature of the buffer layer over y/H=0.01 to 0.05 ($y^+ \approx 5$ to 25). This shows improvement of the near wall velocity measurement relative to Figure 7. The Friction velocity and the wall shear stresses are calculated using the slope of the velocity profiles from the planar PTV data and are shown in Table 2.

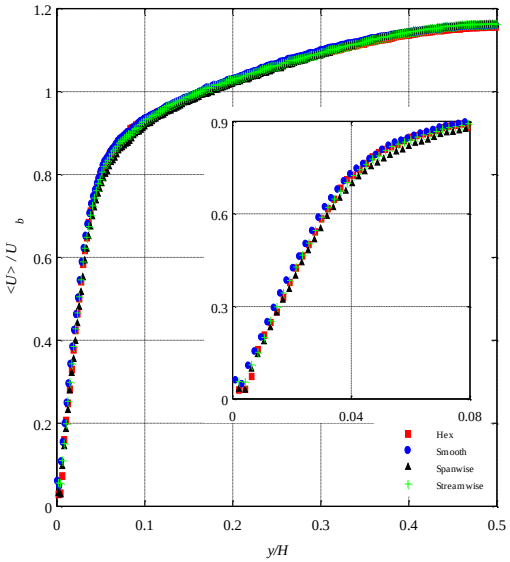

Figure 7. Normalized velocity profiles over the surfaces from ensemble of correlation of LMS images. SHO surfaces are located at y/H=0.

The Reynolds stresses of different surfaces obtained from the planar PIV measurements are all normalized with the friction velocity of the smooth surface and shown in Figure 9. The SHO surfaces are at y/H=0 and the values of $\langle v^2 \rangle$ and $\langle uv \rangle$ Reynolds stresses are multiplied by a factor of 10 for clarity of the figure. The spanwise pattern has the highest Reynolds stresses followed by the hexagonal surfaces. The Reynold stresses of the streamwise surface collapse on the smooth surface. It is also interesting that the existence of SHOs has changed the turbulent intensities on the other wall of the channel. The total wall stress at y/H = 0 can be estimated from extrapolation of a linear fit on the $\langle uv \rangle$ curve over the central region, where the distribution is linear. The results show that the spanwise microgrooves produce the highest wall shear stress. The hexagonal surface has a slightly higher wall shear stress in comparison to the streamwise and the smooth surfaces.

The higher Reynolds stresses and the slightly smaller mean velocity over the spanwise and hexagonal surface shows that air layer is not maintained during the experiments and SHO surfaces became wetted. The behavior of the spanwise and the hexagonal wetted surfaces is similar to a rough wall increasing the wall shear stress. It is also expected the streamwise surface to be also wetted as no reduction of wall shear stress is observed. The wetted streamwise surface performs similar to a riblet surface with undersized grooves (groove width of approximate λ). The

groove width of the riblets is far away from the optimum size (~15λ) which renders the surface as hydrodynamically smooth. The failure of the air layer and formation of wetted surfaces might be due to high shear rate of the turbulent flow removing the air pockets or the silane coating of the SHO surfaces.

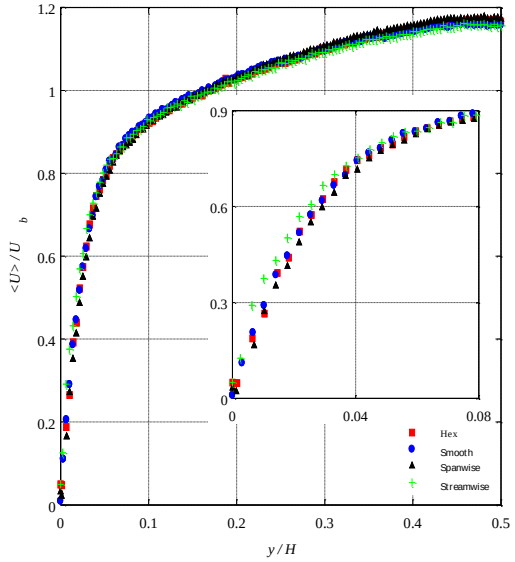

Figure 8. Normalized velocity profile from planar PTV. The labels are similar to Figure 7.

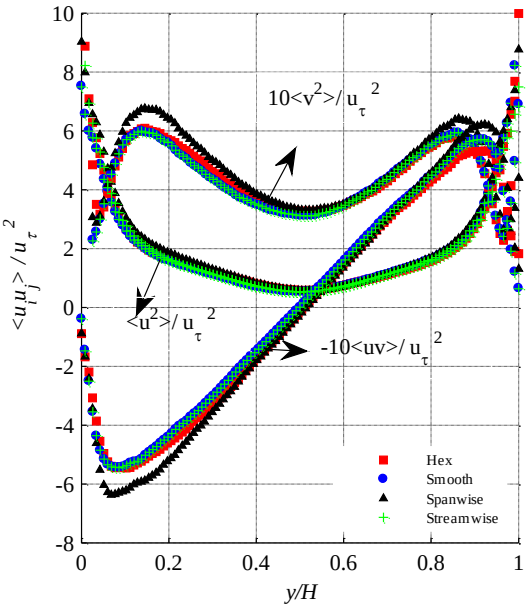

Figure 9. Normalized Reynold stresses over SHOs across the channel obtained from planar PIV.

Table 2. Details of the channel flow.

	Smooth	Hex	Streamwise	Spanwise
U_b, m/s	1.030	1.03	1.027	1.034
u_τ, m/s	0.067	0.073	0.078	0.069
τ_w, kg/(ms^2)	4.482	5.321	4.86	6.074

Volumetric PIV and PTV

In order to investigate the effects of SHO surfaces on the three dimensional turbulent structures, Tomo-PIV and 3D-PTV measurements are considered. The normalized mean velocity profiles across the channel are shown in Figure 10. The point cloud of the 3D-PTV vector field was averaged over the spanwise and streamwise directions followed by averaging over 12 pixel wall-normal windows for faster statistical convergence. The current Tomo-PIV and 3D-PTV results are only based on ensemble of 100 and 500 image pairs, respectively. Considering the ensemble size, the results have not achieved full statistical convergence with the possibility of future improvement. Both techniques show similar velocity profiles. However, the 3D-PTV process has more accurately captured the near-wall velocity gradient ($y/H < 0.2$ or $y/H > 0.8$) due to its higher spatial resolution.

The profiles of Reynolds stress from Tomo-PIV and 3D-PTV are shown in Figure 11. The lower spatial resolution of the Tomo-PIV underestimates the Reynolds stresses in comparison with the planar PIV data of Figure 9 and also the DNS of Kim et al. (1987) according to Pope (2000) at Re=13,750. The DNS data shows the maximum $\langle u^2\rangle/u_\tau^2$ and $\langle v^2\rangle/u_\tau^2$ of about 7.5 and 1, respectively. The 3D-PTV shows higher accuracy in measurement of $\langle u^2\rangle$ and $\langle v^2\rangle$ components. However, the spanwise component $\langle w^2\rangle/u_\tau^2$ of 3D-PTV is overestimated by about 60 percent relative to the $\langle w^2\rangle/u_\tau^2$ =1.75 of Kim et al. (1987).

CONCLUSION

SHO surfaces with micro-size streamwise, spanwise and hexagonal features were fabricated using lithography technique. A planar PIV system is applied to capture the full channel height. The details of the mean velocity profiles are obtained using ensemble of correlations while the turbulent intensities are obtained using individual correlation of double-frame images. A high magnification system is also applied for accurate near wall characterization using PTV. The results show that the air layer was not maintained during the experiments and the surfaces became wetted. The spanwise and the hexagonal surfaces performed as a rough wall slightly decreasing the mean velocity with considerable increase of Reynolds stresses and the wall shear stress. However, the surface with streamwise micro-grooves performed as a highly undersized riblet with no-effect on the turbulent flow.

Tomo-PIV and 3D-PTV measurements were also evaluated over the smooth surface for future characterization of three-dimensional flows over SHO surfaces. The 3D-PTV showed more accurate estimation of $\langle u^2\rangle$ and $\langle v^2\rangle$ in comparison to the Tomo-PIV due to higher spatial resolution. The 3D-PTV overestimates the $\langle w^2\rangle$

component due to higher uncertainty in particle detection in the depth direction.

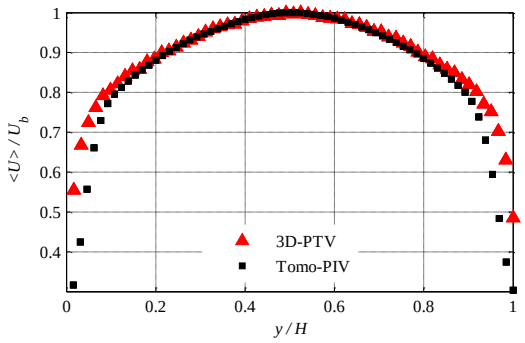

Figure 10. Normalized mean velocity profile from Tomo-PIV and 3D-PTV over the smooth wall.

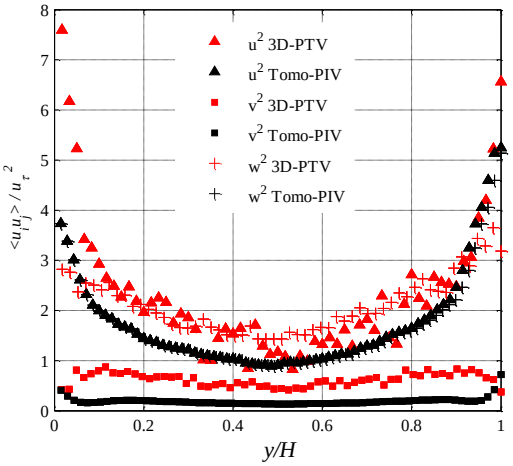

Figure 11. The components of normal Reynolds stresses from the tomo-PIV and 3D-PTV measurements over the smooth wall.

ACKNOWLEDGMENTS

The authors thank professor David Nobes for his advice on the design of water channel facility. This work has been supported by the Natural Sciences and Engineering Research Council of Canada (NSERC RGPIN 1512 GHAEMI).

REFERENCES

Choi, C-H, Ulmanella, U, Kim, J., Ho, C-M, Kim, C-J, 2006, "Effective slip and friction reduction in nanograted superhydrophobic microchannels", *Phys Fluids* 18, 087105.

Davis, J., Maynes, D., Webb, B.W., Woolford B., 2006, "Laminar Flow in micro-channel with Superhydrophobic Walls Exhibiting Transverse ribs", *Physics of Fluid*, 18, 087110.

Elsinga, G.E., Scarano, F., Wienke, B., and Van Oudheusden, B.W., 2006, "Tomographic Particle Image Velocimetry ", *Experiments in Fluids 41*, PP 933-947.

Henoch, C., Krupenkin, T.N., Kolodner, P., Taylor, J. A., Hodes, M. S., Lyons, A.M., Peguero, C., Breuer, K., June 2006, "Turbulent Drag Reduction Using Superhydrophobic Surfaces", *3rd AIAA Flow control conference*, San Francisco, California.

Herman GT, Lent A (1976) Iterative reconstruction algorithms. *Comput Biol Med*., Vol 6, pp. 273-294.

Hyunwook, P., Hyungmin, P., Kim, J., 2013, "A numerical study of the effects of superhydrophobic surface on skin-friction drag in turbulent channel flow", *Phys Fluid*, Vol. 25, 110815.

Daniello, R.J., Waterhouse, E., Rothestin, N.P., Jonathan, 2009, "Drag reduction in turbulent flows over superhydrophobic surfaces", *Phys Fluid*, Vol. 21, 085103.

Kähler, C.J, Scharnowski.S, Cierpka ,C , 2012, "On the uncertainty of digital PIV and PTV near walls", *Exp Fluids*, Vol. 52, pp. 1641–1656

Kim, K. and Kim, C.J., Jan. 2002, "Nanostructured surfaces for dramatic reduction of flow resistance in droplet-based microfluidics", *proceeding of the IEEE conference on MEMS*, Las Vegas, NV, PP. 479-482.

Kim, J., Moin, P., Moser,, R. 1987, "Turbulence statistics in fully developed channel flow at low Reynolds number", *J . Fluid Mech.*, Vol. 177, pp. 133-166.

Lauga, E., Stone. H.A., 2003, "Effective slip in pressure-driven stokes flow", *J. Fluid Mech.* 489, 55.

Martell, M.B., Perot, J.B., Rothestin, J.P., 2009, "Direct numerical simulation of turbulent flow over ultra-hydrophobic surfaces", *Journal Fluid Mechanics*, 620, 31.

Maynes, D., Jeff, K., Woolford, W., Webb, B.W., 2007, "Laminar flow in micro-channel with hydrophobic surface patterned micro-ribs oriented parallel to the flow direction", *Physics of Fluid*, Vol. 19, 093603.

Meinhart, C.D., Wereley, S.T., Santiago, J G, 2000, "A PIV Algorithm for Estimating Time-Averaged Velocity Fields", Journal of Fluids Engineering, Vol. 122 Õ 285 Min, T., Kim, J., 2004, "Effect of hydrophobic surface on skin-friction drag", *Physics of Fluid*, Vol. 16, pp 55-58.

Oue, J., Rothestin, J.P., 2005, "Direct velocity measurement of the flow past drag reducing ultrahydrophobic surfaces", *Phys Fluid*, Vol. 17, 103606.

Park, H., Sun, G., & Kim, C. J., 2014. "Superhydrophobic turbulent drag reduction as a function of surface grating parameters," *Journal of Fluid Mechanics*, Vol 747, pp. 722-734.

Pope, S. B., 2000. "Turbulent flows", Cambridge university press.

Rothstein, J.P., 2010, "Slip on Superhydrophoic Surfaces", *Annu. Rev. Fluid Mech.*, 42:89-109

Watanabe, K., Yanuar, and Udagawa, H., 1999, "Drag reduction of Newtonian fluid in a circular pipe with highly water repellent wall, *J. Fluid Mehc*, 381, pp. 225-238.

Wienke, B., 2008, "Volume self-calibration for 3D particle image Velocimetry, *Experiments in Fluids 45*, pp. 49-55622.

Zhang, H.Q., Fey, U., Noack, B.R., Konig, M., and Eckelmann, H. (1995) "On the transition of the cylinder wake," *Physics of Fluids*, Vol. 7, pp. 779-794.

Zhang, J., Yao, Z., , Hao, P., Tian, H., Jiang, N. , "Fluid drag-reducing effect and mechanism of superhydrophobic surface with micro-nano textures", 4th Micro and Nano Flows Conference, UCL, London, UK, 7-10 Sept. 2014.